Supplementary Information for

Gas-Phase Synthesis of the Bicyclic Silicon Tricarbide Molecule (c-SiC_3) as a Precursor to Silicon Carbide Nanoparticles in Space

Shane J. Goettl, Kazuumi Fujioka, Márcio O. Alves, Mateus X. Silva, Zhenghai Yang, Surajit Metya, Iakov A. Medvedkov, Tosaporn Sattasathuchana,* Breno R. L. Galvão,* Rui Sun,* Ralf I. Kaiser*

*Corresponding author: Ralf I. Kaiser, ralfk@hawaii.edu; Rui Sun, ruisun@hawaii.edu; Breno R. L. Galvão, brenogalvao@gmail.com, Tosaporn Sattasathuchana, tsatta@hawaii.edu

Experimental methods

The reactions of tricarbon (C_3, $X^1\Sigma_g^+$) with the silylidyne radical (SiH, $X^2\Pi$) were conducted under single collision conditions utilizing a crossed molecular beams machine.[1] Briefly, a pulsed supersonic tricarbon beam was produced *in situ* via laser ablation of a rotating graphite rod using the fourth harmonic of a Nd:YAG laser (Quanta-Ray Pro 270, Spectra-Physics) at 30 Hz and 2–5 mJ per pulse. The ablated species were seeded in neat helium gas (He, 99.9999 %, Matheson) at a backing pressure of 3,000 Torr. The reactant beam was skimmed then velocity-selected by a four-slot chopper wheel with a peak velocity (v_p) of 1754 ± 27 m s^{-1} and speed ratio (S) of 5.0 ± 0.3. A pulsed beam of silylidyne radicals was prepared via photolysis of disilane (Si_2H_6, 99.998%, Air Liquide) seeded in helium (He; 99.9999%; Matheson) at a fraction of 0.5% and a backing pressure of 1.5 atm.[2] This gas mixture was fed into a piezoelectric valve operating at 60 Hz, −400 V amplitude, and a pulse width of 80 μs, and the released pulsed beam was intercepted by a 1 mm × 4 mm laser spot from a 193 nm ArF excimer laser (COMPex 110, Coherent) of 30 Hz and 15 mJ per pulse, which was located 1 mm downstream from the nozzle.

The tricarbon beam crossed perpendicularly with the silylidyne beam (v_p = 1698 ± 8 m s^{-1}, S = 16.3 ± 2.2) granting a collision energy (E_c) of 47.9 ± 0.9 kJ mol^{-1} and CM angle (Θ_{CM}) of 38.7 ± 0.6°. It is important to note that both carbon atoms (C) and dicarbon molecules (C_2) are also produced in the laser ablation process of the primary beam, and photolysis of disilane in the secondary beam can also produce silane molecules (SiH_4) and silyl radicals (SiH_3).[3,4] The lower masses of 12 and 24 amu for carbon and dicarbon compared to tricarbon, respectively, indicate that products observed in the title reaction cannot be produced from the reactions of carbon/dicarbon with silylidyne, silyl, or silane. Possible reactions of carbon and dicarbon with disilane would produce the collision complexes CSi_2H_6 (74 amu) and $C_2Si_2H_6$ (86 amu); however, there are no possible fragments which can give signal at m/z = 64 observed for the title reaction. Additionally, the tricarbon molecule was found not to react with silane or disilane under our experimental conditions.

Reactively scattered products were collected by a triply differentially pumped mass spectrometric detector which is rotatable in the plane defined by both reactant beams. Products were ionized by electron impact ionization at 80 eV and emission current of 2 mA before mass filtering via a quadrupole mass spectrometer (150QC, Extrel) operating in the time-of-flight (TOF) mode. Up to 5.2 × 10^6 TOF spectra were collected at each angle in 5° steps for the range 25° ≤ Θ ≤ 59° with respect to the tricarbon beam (Θ = 0°). Integrating the TOFs and normalizing to the CM angle created a laboratory angular distribution (LAD). In order to obtain information on the chemical dynamics, the laboratory data were fit using a forward convolution routine, in which user-defined CM translational energy ($P(E_T)$) and angular ($T(\theta)$) flux distributions were refined iteratively until a reasonable fit of the data was achieved.[5,6] The image of the overall outcome of the reaction was developed from these functions, defined as $I(u,\theta) = P(u) \times T(\theta)$, and is portrayed as a flux contour map.[7]

Computational methods

The electronic structure calculations performed for constructing the SiC_3H potential energy surface were carried out employing the MOLPRO[8] package. Geometry optimizations on the reactants, products, intermediates and transition states were performed with density functional theory and using the TPSSh functional[9] with the aug-cc-pV(T+d)Z[10] basis set. For all optimized structures, vibrational frequencies calculations were performed with the same methodology from where zero-point energies are extracted. To enhance the accuracy of the energies obtained, we have performed single-point energy calculations on all optimized structures using the explicitly correlated coupled cluster method with single, doubles plus perturbative triples excitations[11,12] (CCSD(T)-F12) with the aug-cc-pV(Q+d)Z basis set. The notation used to express this overall approach is therefore CCSD(T)-F12/aug-cc-pV(Q+d)Z//TPSSh/cc-pV(T+d)Z + ZPE (TPSSh/cc-pV(T+d)Z).

Electronic structure calculations with different levels of theory were screened to choose a benchmark method for *ab initio* molecular dynamics (AIMD) simulations and the results are shown below. AIMD simulations were run with VENUSpy/PSI4[13,14] using m11/cc-pVDZ[15-17] with the velocity Verlet integrator and a timestep of 0.15 fs. The rotation and vibration of reactant molecules were sampled from a canonical 10 K ensemble for C_3 and the ground state for SiH. The two reactant molecules were separated by 10 Å with random orientations and set to collide with an energy of 47.9 kJ mol^{-1}. The initial sampling of the reactants mimicked the experimental conditions. 100 trajectories were carried out at discrete impact parameters for b = 1.0 Å, 2.0 Å, … up until a maximum value where none of the trajectories were reactive (i.e., all trajectories reformed reactants without forming intermediates). To make the calculation feasible, each trajectory was allowed to run for up to three days with an average time of 2.2 ps per trajectory. Trajectories that did not preserve the total energy were allowed to restart at least twice to simulate a minimum of 0.5 ps before being replaced with a new trajectory started with a different set of initial coordinates and momenta.

Frames (molecular geometries, energies, and energy gradients) with unique geometries from the AIMD simulations were used to build a training set to develop a machine learning (ML) potential. The uniqueness of the geometries was determined with a distance matrix deviation (DMD).[18] Of the roughly 10 million frames visited in the AIMD simulations, 15,454 frames were selected. The symmetrized gradient domain machine learning (sGDML) method[19] was ultimately chosen and the final model was fit with a regularization of 10^{-10} and length scale of 15. More details on the development of the sGDML potential can be found below. Machine-learned molecular dynamics (MLMD) simulations were run with VENUSpy/sGDML, with the same initial sampling as AIMD simulations. 300 trajectories were carried out at discrete impact parameters for b = 0.5 Å, 1.0 Å, … up until a maximum value where no reactions occurred. Trajectories were allowed to run for up to 15 ps.

The mechanism of the reactions was described by a semi-Markov model. The first step of this process was to identify an International Chemical Identifier (InChI) code[20] to each frame of the trajectory. To accommodate for the larger bond distances seen in the trajectories, the bond distance threshold scale was increased from the default value of 1.25 to 1.35, which was used to generate a structure-data file (SDF) and then converted to an InChI code with Open Babel.[21] Various thresholds for atom-atom distances in the InChI code were tested and 1.35 produced intermediate categorizations that were the most reasonable over AIMD trajectories. In our experience, the bond distance threshold in InChI should be determined case-by-case, as it is determined by the nature of the reaction system as well as the level of excitation. Further analysis on this threshold is outside of the scope of the current study, so details are not listed here. These InChI codes were then related to the InChI code of the intermediates on the potential energy surface. If certain InChI codes appeared repeatedly but did not match any intermediates, they were defined as

metastable state(s). As such, the trajectories could be reduced into a series of transitions between intermediates and, if necessary, metastable states. Steady state solutions for the semi-Markov model require an inverse Laplace transform (ILT) of a non-analytical function. The ILT was calculated numerically by a reformulation of the integral as a regularized non-negative least squares (RNNLS) problem[22] using 80 points over the range [10^{-2}, 10^{10}] fs and a regularization of 10^{-8}.

The quasi-atomic orbital (QUAO) analysis[23-26] was performed using the GAMESS[27-30] software package to extract bond motifs in three SiC_3 isomers. Since the method is independent of basis set and derived based on wavefunction theory,[31-33] the localized quasi-atomic orbitals were computed at the restricted open-shell Hartree Fock (ROHF) wavefunction with aug-cc-pV(T+d)Z basis set at the TPSSh/cc-pV(T+d)Z optimized geometries.

Details of AIMD Simulations

The setup for *ab initio* molecular dynamics (AIMD) simulation includes a proper level of theory for electronic structure calculations and molecular dynamics (MD) parameters for trajectory propagation. Several combinations of density functional theory (DFT) and basis sets were screened. For each combination, reactants, products, and entrance channel intermediates were optimized. Their energies (with zero-point energy) were then compared with the reference potential energy surface (PES) computed with CCSD(T)-F12/aug-cc-pV(T+d)Z//TPSSh/cc-pV(T+d)Z (Fig. 4 in the manuscript). A summary of this comparison can be seen in Table S1 below.

Table S1. Root mean square errors (RMSEs) between the reference PES energies (E+ZPE, kJ mol^{-1}) to those optimized with various methods. Methods with double zeta basis sets are colored black, and others are colored red. Methods with the lowest errors (< 20 kJ mol^{-1}) are bolded.

Level of Theory	RMSE	Level of Theory	RMSE
B3LYP/6-31G*	26.8	PBE0/6-31G*	32.4
B3LYP/cc-pVDZ	31.4	PBE0/cc-pVDZ	25.7
B3LYP/cc-pVTZ	29.3	PBE0/cc-pVTZ	25.7
B3LYP/def2-SVP	29.1	PBE0/def2-SVP	36.7
BNL/cc-pVDZ	**17.2**	SOGGA-11x/6-31G*	22.1
m06-2x/6-31G*	27.6	SOGGA-11x/cc-pVDZ	**16.4**
m06-2x/cc-pVDZ	24	SOGGA-11x/cc-pVTZ	22.5
m06-2x/cc-pVTZ	48.3	SOGGA-11x/def2-SVP	27.4
m06-2x/def2-SVP	32	TPSSh/6-31G*	22.9
m11/g-31G*	36.3	TPSSh/aug-cc-pVDZ	**18.7**
m11/cc-pVDZ	**14.9**	TPSSh/aug-cc-pVTZ	21.7
m11/cc-pVTZ	**14.9**	TPSSh/cc-pVDZ	20.3
m11/def2-SVP	40.4	TPSSh/cc-pV(T+d)Z	23.1
rCAM-B3LYP/cc-pVTZ	38.6	TPSSh/cc-pVTZ	21.9
rev-m06/cc-pVTZ	26.7	TPSSh/def2-SVP	26

Table S1 serves as a primary screening for a relatively large number of levels of theory. Of these, m11/cc-pVDZ was chosen due to its relatively low error compared to other candidates and speed, as well as consistency between the DZ and TZ basis set. It is important to note that for AIMD simulations, choosing a fast method is important to enable the millions of energy gradient calculations needed in trajectories, thus TZ basis sets were unfavored unless the accuracy gain outweighs the additional computational cost. MP2 optimizations were also attempted but for every basis set, there

was at least one stationary point that could not be successfully optimized. m11/cc-pVDZ was further applied to all stationary points on the reference PES, resulting in an RMSE of 14.1 kJ mol^{-1}. This level of agreement is within the range of errors reported in AIMD simulations of similar reactions.[34]

Any AIMD trajectories that result in non-reaction (C_3 + SiH) or product formation (SiC_3 + H or C_3H + Si) are stopped after the centers of mass of the two molecules are more than 14 Å apart. Otherwise, trajectories are run for three days. At each step of the AIMD trajectories, the total energy is computed and monitored for energy jumps (absolute deviations between steps) and energy drift (absolute deviation relative to the beginning of the trajectory). If either exceeds 1.0 kcal mol^{-1} or if there is an SCF error, depending on the length of the trajectories, there are different reviving strategies. For longer (e.g., over 0.5 ps) trajectories, they are given a chance to restart from the frame before the error with a superposition of atomic densities (SAD) guess. For shorter (e.g., less than 0.5 ps), they are given two chances to restart from the beginning of the trajectories with two smaller integration time steps. If a trajectory is still problematic after the reviving attempts, it will be replaced with a new trajectory.

Benchmarking the sGDML potential for Reaction Dynamics Simulations

In all simulations in this manuscript, the reactants (C_3 + SiH) are set to collide with a collision energy of 47.9 kJ mol^{-1}. The rotational and vibrational energies of the reactant species are sampled to match experimental conditions. As a first effort of exploring the dynamics of the reaction, 600 bimolecular collision *ab initio* molecular dynamics (AIMD) trajectories were simulated for 3 ps or until dissociation to reactants or products, but only 16 formed bimolecular products. This is due to the deep potential energy well in the entrance channel (e.g., **i1**) as well as highly endothermic dissociation (e.g., **i8** to **p1**). Although the system possesses enough energy to eventually dissociate, the timescale of such dissociation is not accessible in AIMD simulations. Similar phenomena have been reported in other bimolecular collisions with a deep entrance channel as well.[34,35] Therefore, an sGDML potential was developed to assess longer time scales. The validity of the sGDML potential was extensively benchmarked against AIMD simulations.

For most machine-learned (ML) potentials to date, there is in general no guarantee of accuracy outside the training set (i.e., "extrapolation"). Therefore, at least in theory, the training set must cover the entire chemical space that may be visited in the actual dynamics simulations up to a certain resolution (i.e., "interpolation"). In the current study, the training set is gathered from AIMD simulations. Although the potential energy obtained from AIMD simulations is generally more continuous than discrete *ab initio* calculations, it remains impossible to rule out discontinuities. For example, radical H + singlet SiC_3 and radical H + triplet SiC_3 are both doublet solutions to m11/cc-pVDZ in AIMD simulations with different S^2 value, but singlet SiC_3 is expected to have a different potential energy landscape compared to triplet SiC_3. If both channels were observed in AIMD simulations and included in the training set, discontinuity is introduced.

To mitigate this discontinuity problem, 100 trajectories are simulated at impact parameters 1.0 Å and 2.0 Å with a mixed integration scheme, using an *ab initio* – sGDML hybrid surface. Since the sGDML potential is inherently continuous, a local sGDML potential is developed on-the-fly when energy or SCF errors occur. The sGDML potential aims to surf the simulation through the rough regions on the *ab initio* surface. This special type of AIMD simulation could be generated with the latest development version of VENUSpy.[13] Out of the roughly 4 million geometries visited

from the 200 trajectories, a diverse set of 18,954 distinct geometries are chosen by distance matrix deviation as the *preliminary* training set. A preliminary, *global* sGDML potential energy surface is developed with this training set and serves the purpose of further filtering discontinuous frames from the AIMD simulations. Here, a conservative approach was taken with the assumption that the preliminary *global* sGDML surface is a reasonable approximation of the final sGDML surface, that is close to the true, continuous, *ab initio* surface. Therefore, the *ab initio* frames in the training set that have a large deviation in energy or gradient from the preliminary sGDML surface should be excluded from developing the final sGDML surface, as they would be discontinuous from the rest of the training set. Fig. S1 shows the errors in energy and gradient between the preliminary sGDML surface and their *ab initio* counterpart in the training set.

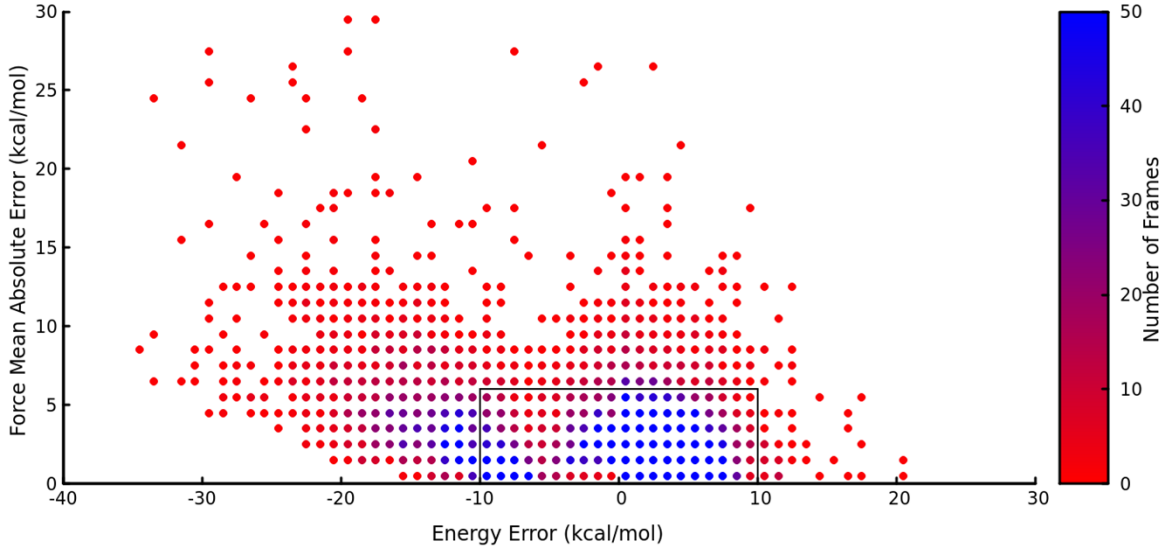

Fig. S1. Energy and force errors for each point in the initial training set before filtering, calculated from a rough ML surface. Regions on the energy-force error graph with more than 50 frames exist and are colored blue.

For this research, the *preliminary* training set is filtered with the cut-off of 10 kcal mol^{-1} in energy error and 6 kcal mol^{-1} $Å^{-1}$ in energy gradient error to make the *final* training set. This filtering removed 18.5% of the frames, leaving the *final* training set with 15,454 frames, whose energies range over 118 kcal mol^{-1} and energy gradients range over 1,130 kcal mol^{-1} $Å^{-1}$. Most (78%) of these frames are in the unimolecular region of the PES. Over the bimolecular region of the PES, four product channels (**p1**, **p2**, **p3**, and **p4**) make up about 13% of the training set compared to the 9% corresponding to the reactant channel. The distribution of energies in the final training set is best shown with a t-distributed stochastic neighbor embedding (t-SNE) representation, shown in Fig. S2 (left). The intermediates (unimolecular) species (Fig. S2 right panel: C_3HSi points, colored purple) cover a wide range of energies, gradually transitioning to high-energy regions (Fig. S2 left panel: left, top left) which correspond to the high-energy reactant (C_3 + HSi) and product channels (C_3Si + H and C_3H + Si).

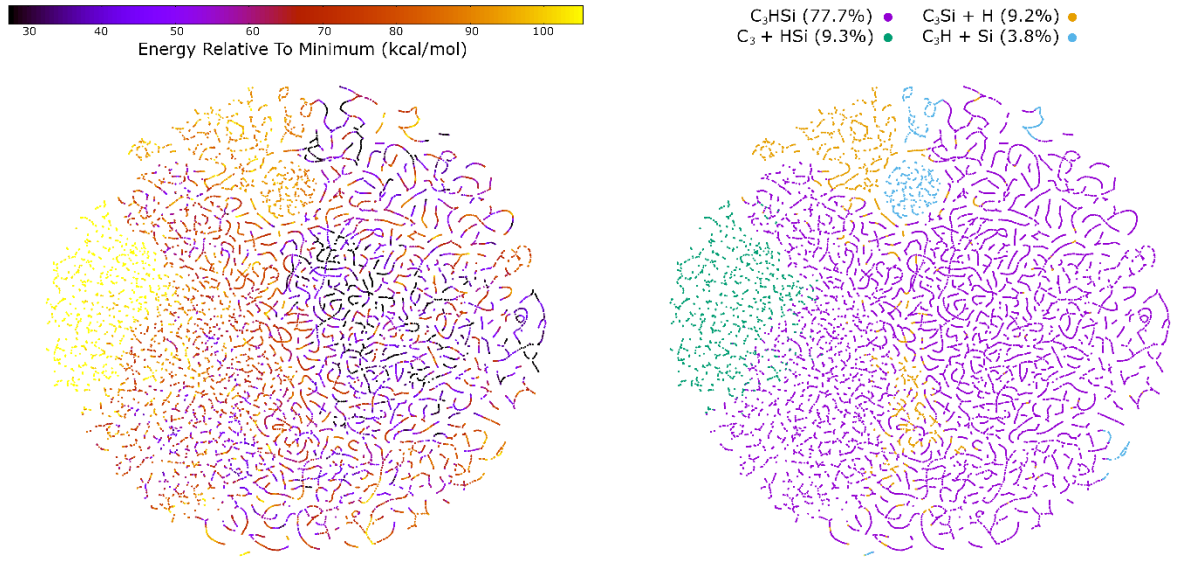

Fig. S2. A t-distributed stochastic neighbor embedding (t-SNE) representation of the training set with each of the 15,454 frames represented as a point. The t-SNE was constructed using pairwise DMD values. On left, points are colored by their energy relative to the global minimum. On right, points are colored by categorization of molecules into reactant/product and bimolecular/unimolecular.

The *final* sGDML potential energy surface was developed with a regularization of 10^{-10} and length scale of 15. These hyperparameters were picked after scanning over length scales of 5 to 50 with the conjugate gradient solver. Larger training sets were also attempted, but they were too memory-costly with the analytical solver or too time-consuming with the conjugate gradient method. The final sGDML surface has static energy errors of 0.94/2.27 (MAE/RMSE) kcal mol^{-1} and force errors of 0.62/1.27 (MAE/RMSE) kcal mol^{-1} $Å^{-1}$. As have been well-documented in recent research, an ML-based surface should be benchmarked against AIMD simulations.[18,35] First, we compared the reaction probability (i.e., forming intermediates or products after collision) vs impact parameter, with results shown in Fig. S3. As the figure shows, MLMD is able to recreate the AIMD results qualitatively for all impact parameters. Their resulting total cross sections also agree within a 95% confidence interval.

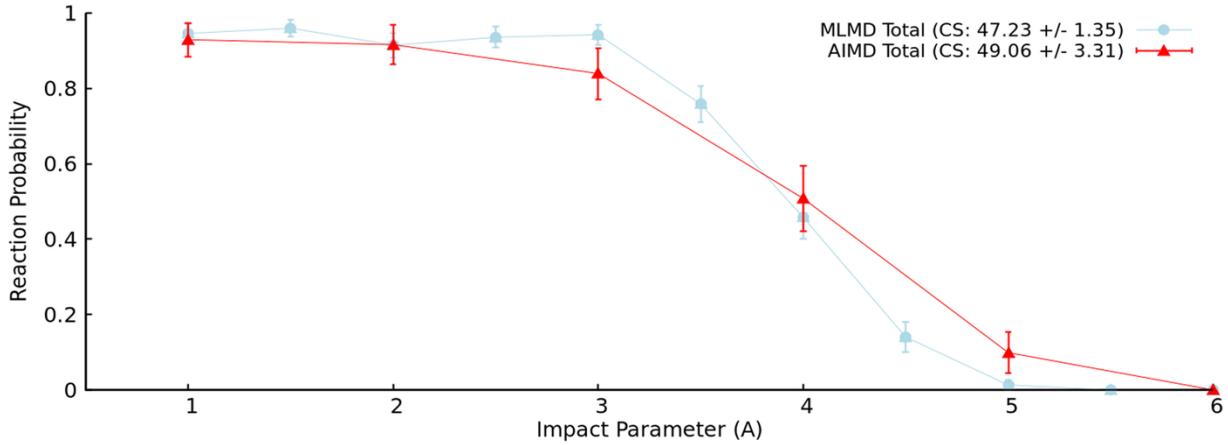

Fig. S3. The reaction probability as a function of impact parameter (P(b)) for intermediate formation ("Total") for the AIMD and the MLMD. Cross sections (CS) are shown in the key. Reaction probabilities and cross sections are presented with +/- 95% confidence intervals.

To see the differences in isomerization dynamics among intermediates in more detail, the transition probabilities of the AIMD and MLMD simulations can be directly compared. For discrete probability distributions like those over the transitions, continuous metrics like the Kolmogorov-Smirnov deviation (KSD) cannot be used. A common metric used for discrete probability distributions (p_{ij}) is the Kullback-Leibler divergence (DKL), which, for the transition probabilities, are DKL(AIMD || MLMD) = 0.1138 and DKL(MLMD || AIMD) = 0.0973. However, there is no standard error for the DKL values. If instead, the Bernoulli standard error ($SE_{ij} = \alpha \sqrt{\frac{p_{ij}(1-p_{ij})}{N_{ij}}}$, for an α confidence interval and a N_{ij} number of recorded transitions) is computed, treating the transition probabilities as a multinomial distribution, including reactants, of the 156 possible transitions, 128 fell within the 95% confidence intervals.

Complete MLMD Results

The MLMD reactive trajectories exhibited a total reactive cross section of 47.23 Å^2. The reactivity can be further explored as a function of impact parameter, as shown in Fig. S4.

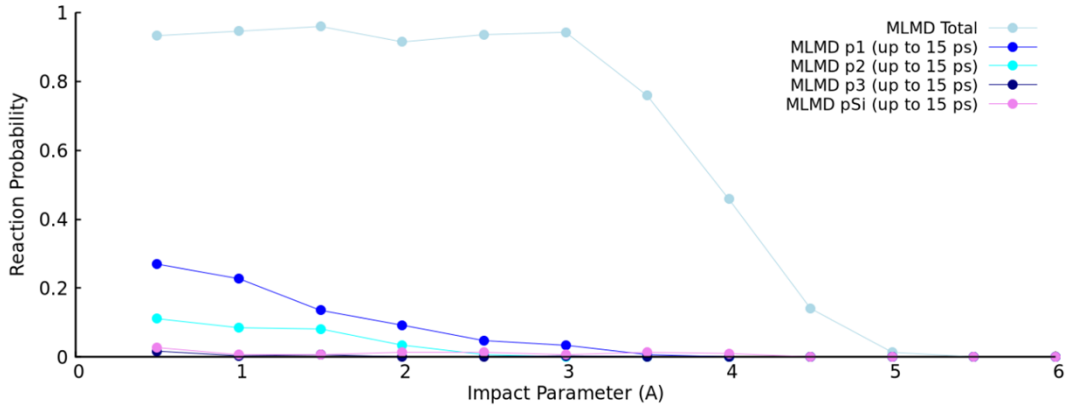

Fig. S4. The reaction probability as a function of impact parameter (P(b)) for intermediate formation ("Total") and for each product channel (**p1**, ..., **p4**).

Complete breakdowns of transition probabilities $p_{ij} = P(j|i)$ of species i isomerizing to species j are detailed below as percentages in Table S2:

Table S2. Transition probabilities, represented as percentages, for each species-species transition. Probabilities from each species (those in the same row) sum to unity (100%).

	i1	**i2**	**i3**	**i12**	**m1**	**i11**	**i4**	**i5**	**i6**	**i8**	**i10**	**i9**
r	87.74	4.83	0.04	2.95	3.6	0	0	0.83	0	0	0	0
i1	0	3.69	1.08	54.79	37.67	0.07	0.26	2.16	0.03	0	0.24	0.01
i2	37.72	0	12.31	2.46	0.33	0.07	0.87	40.79	0.09	0.01	4.56	0.07
i3	5.19	4.82	0	0.53	75.56	0.24	12.02	0.73	0	0.01	0.01	0
i12	40.97	0.18	0.11	0	4.2	0.41	17.01	34.34	0.01	0.04	0.58	2.15
m1	58.88	0.04	28.97	8.31	0	2.2	1.54	0.04	0	0	0.01	0
i11	0.02	0	0.03	0.33	0.64	0	28.35	0.21	0.15	42.46	27.74	0.01
i4	0.17	0.09	1.95	14.85	0.64	33.95	0	32.96	0.94	9.84	0.81	3.66
i5	0.99	1.95	0.12	22.38	0.02	0.18	26.67	0	1.96	1.5	36.24	7.93
i6	0.06	0.09	0.02	0.05	0	1.49	7.8	21.66	0	66.91	1.92	0.01
i8	0.01	0.01	0	0.05	0	65.54	12.68	2.48	10.18	0	8.94	0
i10	0.26	0.32	0.01	0.51	0.01	37.79	1.01	51.75	0.37	7.93	0	0.02
i9	0.04	0.04	0	11.12	0	0.04	24.03	64.51	0	0.03	0.18	0

	p1	**p2**	**p3**	**p4**
r	0	0	0	0
i1	0	0	0.01	0
i2	0	0.72	0	0
i3	0.89	0	0	0
i12	0	0.01	0	0.01
m1	0.01	0	0	0
i11	0.01	0	0	0.05
i4	0.11	0	0	0.01
i5	0	0.06	0	0
i6	0	0.01	0	0
i8	0.1	0	0	0
i10	0	0.01	0.01	0
i9	0	0	0	0

Complete breakdowns of which intermediate species formed each product (**pX**), normalized by conditional probabilities P(**iX**|**pX**), are given below in Fig. S5:

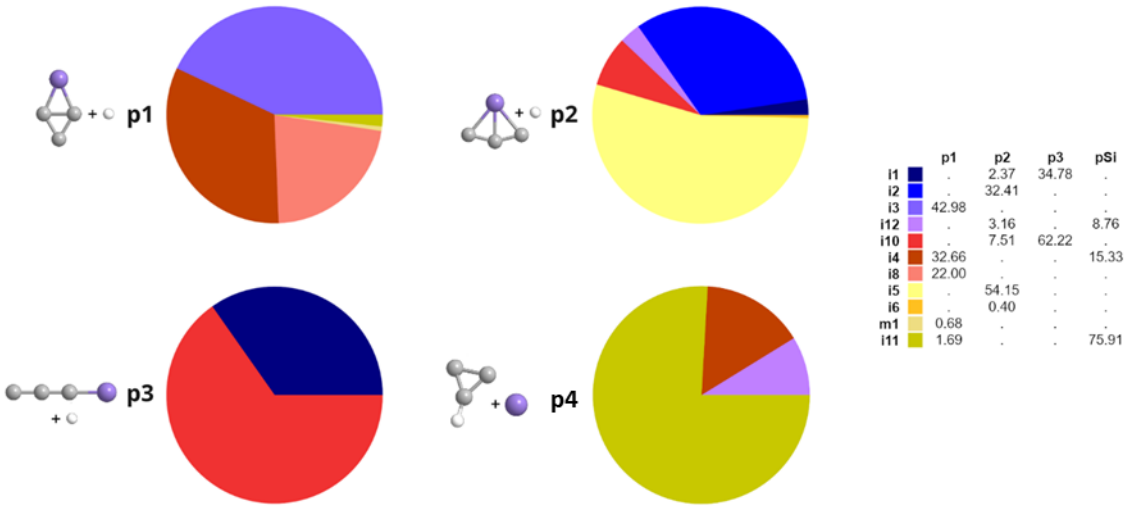

	p1	p2	p3	pSi
i1	.	2.37	34.78	.
i2	.	32.41	.	.
i3	42.98	.	.	.
i12	.	3.16	.	8.76
i10	.	7.51	62.22	.
i4	32.66	.	.	15.33
i8	22.00	.	.	.
i5	.	54.15	.	.
i6	.	0.40	.	.
m1	0.68	.	.	.
i11	1.69	.	.	75.91

Fig. S5. Intermediate-product conditional transition probabilities, represented as percentages, are shown on right. On left, the same data is shown as pie charts. Conditional probabilities to each product (those in the same column) sum to unity (100%).

Details of the Markov state model

A representative diagram of the transitions of the Markov model is shown in Fig. S6, where one bimolecular reactant state, 12 unimolecular states, and 4 product states (**p1**, **p2**, **p3**, and **p4**) are sufficient to describe all trajectories. It is interesting to note that out of the 12 identified Markov states, one state (**m1**) does not correspond to an intermediate, but rather a metastable state similar to the transition state between **i1** and **i3**. This metastable state is frequently observed and the trajectories spend a fair amount of time in this region. In Fig. S6, only transitions with a significant probability are presented, with the most probable transitions from every Markov state colored red. Product formation from a unimolecular state is a rare event, thus the dashed arrows pointing towards the products are the probabilities of formation from the dissociation of a certain unimolecular state.

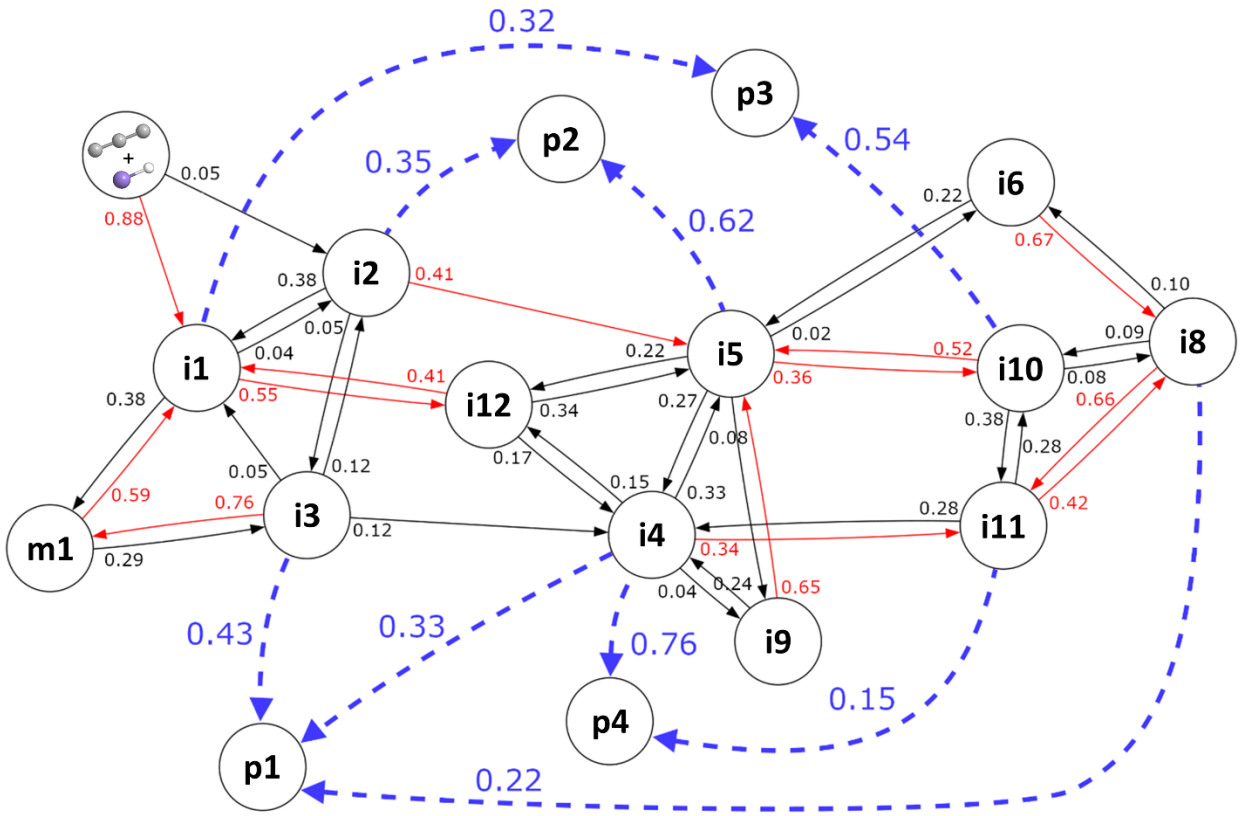

Fig. S6. Markov model transition probability matrix visualized as a digraph, with an arrow from species i to j representing a significant probability p_{ij} = P(i|j) (in black and red). Probabilities out of a node sum to unity. Of all transitions out of a node, the most probable is colored red. Arrows connecting intermediate **iX** to product **pX** represent a significant conditional probability P(**iX**|**pX**) (blue). Conditional probabilities into a product node sum to unity.

As the computational methods section indicates, all species in the Markov model are determined by their InChI connectivity, a geometric descriptor, and confirmed to have significant lifetimes. Note that even if Markov states are named after critical points on the PES (Fig. S7), trajectories do not go through those exact optimized structures due to the excess energy in the system. Instead, traversing through a certain Markov state means that the trajectory is in a configurational space that is closer to the corresponding intermediate than all other intermediates. Technically speaking, any frames in the trajectories can be categorized as an intermediate Markov state, as there must exist a closest intermediate. However, such categorization is meaningless when the configuration of the frame is significantly different from even the closest intermediate. As noted in the computational methods section, all frames are checked against only intermediates and the ones that do not fit are first identified as metastable state. All the frames that are categorized as metastable state are analyzed, and all of them resemble the structure of the self-isomerization of **i3**, noted as **m1** in Fig. S6.

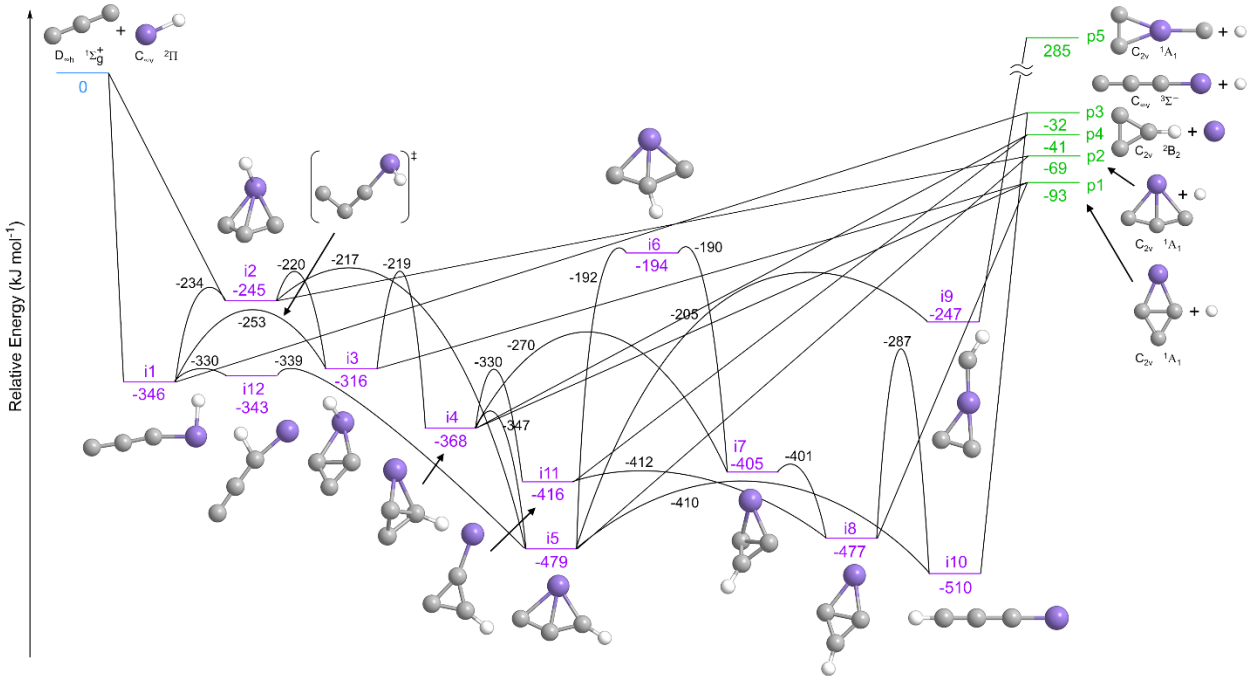

Fig. S7. Schematic PES for the reaction of tricarbon (C_3) with the silylidyne radical (SiH) calculated with density functional theory and using the TPSSh functional with the aug-cc-pV(T+d)Z basis set. Relative energies are given in kJ mol^{-1}, and point groups and electronic states are provided for reactants and products. Energy levels of intermediates are shown in purple and those of products are shown in green.

It is important to note that the Markov model and product distribution is obtained from MLMD simulations of up to 15 ps. Within this time frame, only 11% of the trajectories forming intermediates after collision eventually dissociate to products. The leftover 89% of intermediates will eventually dissociate as the excess energy is above the barriers of the reaction. The fate of these residual intermediates and their resulting final product distribution can be estimated by considering the behavior of unimolecular (intermediate and metastable) species in the long time limit, $t \rightarrow \infty$. The large number of isomerizations from the MLMD simulations serve as the foundation to estimate the lifetime of unimolecular species, $f_{ij}(t)$, for transitions between species i to j. While many of these lifetimes follow a non-Markovian distribution, their time evolution can be solved as a semi-Markov model, and the semi-Markov final product branching ratio can be calculated. The branching ratios change little between what is directly observed from the MD simulations up to 15 ps and what is predicted from the semi-Markov model's asymptotical behavior (i.e., $t \rightarrow \infty$**)**, as shown in Table S3, suggesting additional simulation would not change the results significantly.

Table S3. Calculated product branching ratios from the raw MLMD data ($t < 15$ ps), and from solving for steady states of the semi-Markov model ($t \rightarrow \infty$).

	t < 15ps	**t → ∞**
	MLMD	Semi-Markov
p1	63%	59.0%
p2	22%	24.4%
p3	2%	2.3%
p4	13%	14.3%

Solving for Stationary States of the Markov State Model

Traditionally, final product distributions such as product branching ratios are estimated with rate constants calculated from transition state theory, but here, given the large amount of dynamics data, a statistical estimate can be made from the Markov model. Many traditional results can be obtained from this analysis, as shown in Fig. S8. For example, long-lifetime intermediate concentrations converge to a steady state (left panel) and product formation rates from any single intermediate follow a roughly first-order exponential decay (right panel).

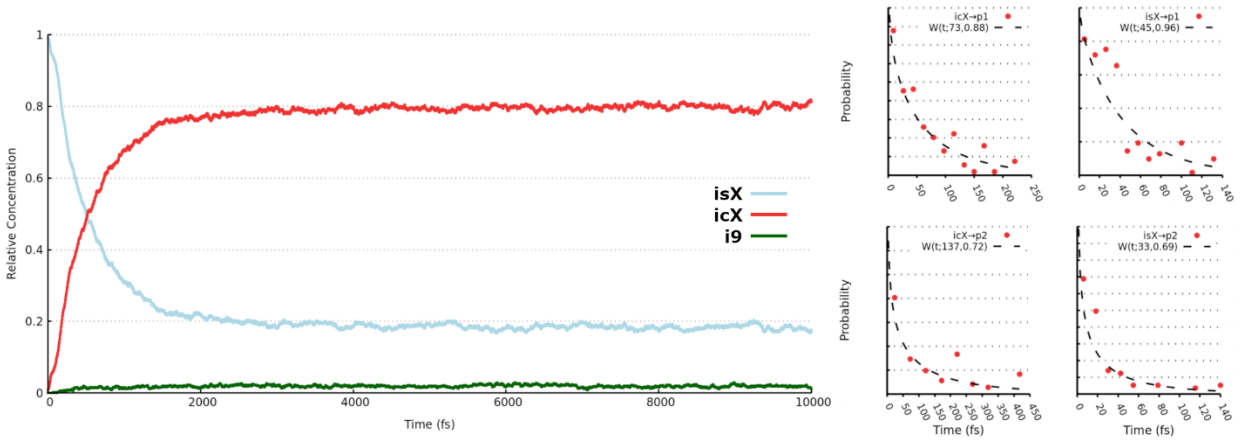

Fig. S8. On left, intermediate concentrations post-collision are shown over time, normalized to sum to unity. Product formation is described broadly through regions: the shallow region of the PES with Si-H motifs (**isX**), the deep region of the PES with C-H motifs (**icX**), and the trapped region of the PES with no possible product formation (**i9**). On right, intermediate-product lifetimes are shown (red points) overlaid with best-fitted Weibull distributions W(t; τ, η).

We can also see intermediate lifetime distributions f_{ij} for intermediate-intermediate isomerizations from species i to j, many of which exhibit significant non-RRKM behavior due to their lower barriers, as shown in Fig. S9 below.

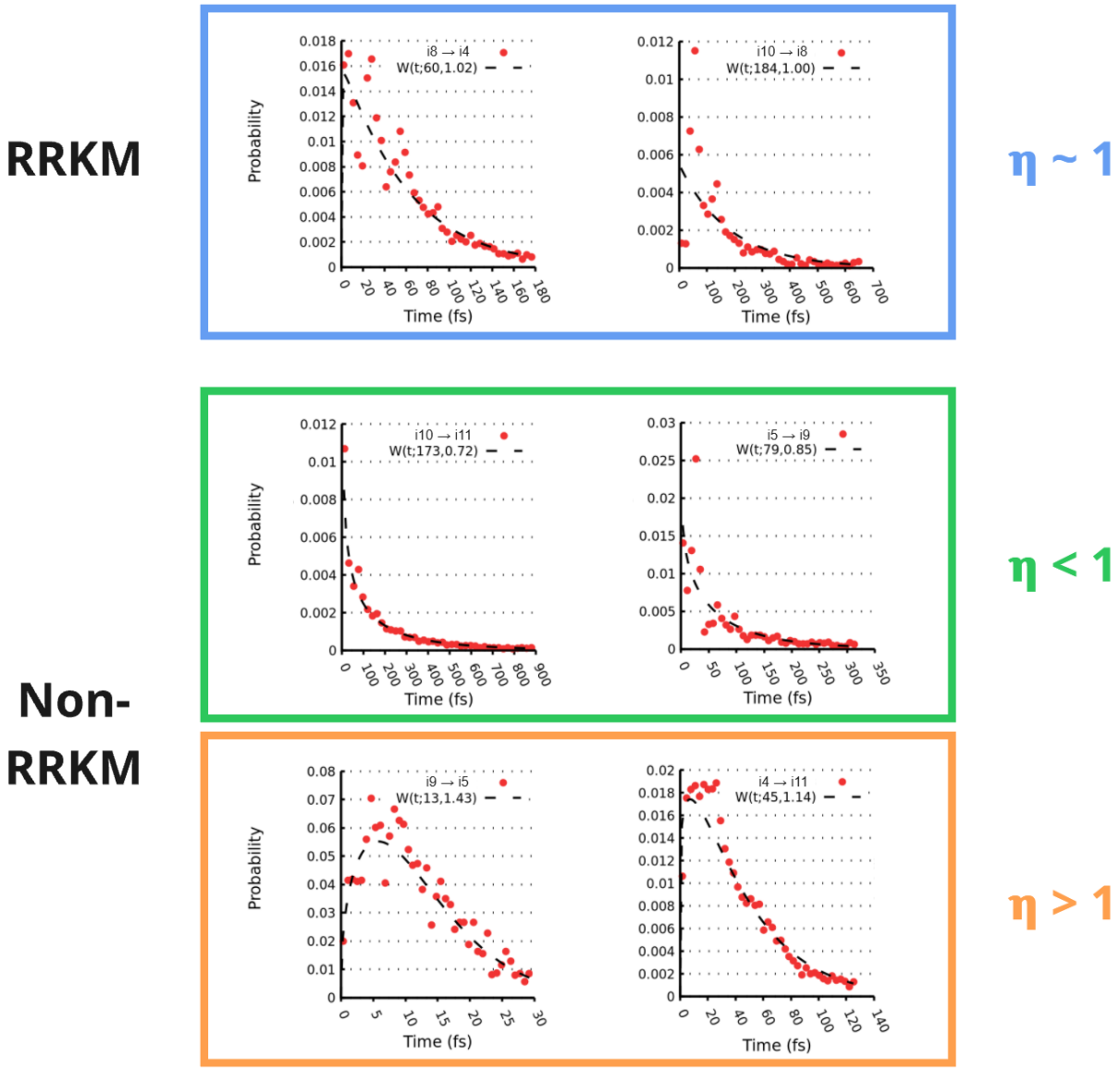

Fig. S9. Distributions of lifetimes for species-to-species transitions are shown (red points) overlaid with best-fitted Weibull distributions W(t; τ, η). From top to bottom, distributions are fit with an ordinary exponential decay less-and-less goodness-of-fit.

Each lifetime distribution $f_{ij}(t)$ is compared to a best-fit Weibull distribution of the following form, which can capture a wide range of both RRKM and non-RRKM behaviour:

$$W(t;\tau_{ij},\eta_{ij}) = \left(\frac{\eta_{ij}}{\tau_{ij}}\right)\left(\frac{t}{\tau_{ij}}\right)^{\eta_{ij}-1} e^{-(t/\tau_{ij})^{\eta_{ij}}}$$

The average intermediate lifetime would then be $\langle t_{ij}\rangle = \tau_{ij}\,\Gamma(1+1/\eta_{ij})$ where Γ is the gamma function. This can be compared with an average lifetime predicted by rate constant theory (e.g., RRKM theory or VTST) as $\langle t_{ij}\rangle = 1/k_{ij}$.

The total set of fitted Weibull parameters for transitions from species i to j which have non-zero probability are shown in Tables S4 and S5, below.

Table S4. The set of fitted Weibull scale parameters τ_{ij} for the transitions from species i to j.

	i1	**i2**	**i3**	**i12**	**m1**	**i11**	**i4**	**i5**	**i6**	**i8**	**i10**	**i9**	**p1**	**p2**	**p3**	**p4**
i1	0	848	508	631	496	731	771	1009	1173	0	1255	0	0	506	1132	0
i2	545	0	363	670	561	0	612	272	359	0	764	0	0	213	0	0
i3	435	419	0	612	402	509	380	652	0	0	600	0	304	0	0	0
i12	368	713	485	0	388	486	522	664	845	731	434	452	0	0	0	351
m1	306	963	466	524	0	497	658	662	0	0	418	0	150	0	0	0
i11	423	0	622	665	474	0	467	862	431	515	291	0	624	0	0	391
i4	607	643	310	525	462	297	0	542	418	309	461	0	298	0	0	703
i5	1417	813	866	943	926	1120	747	0	590	794	1185	525	0	728	0	0
i6	1048	536	0	479	0	223	302	107	0	234	480	0	0	0	0	0
i8	0	621	294	585	0	420	397	575	454	0	649	0	852	0	0	0
i10	2774	2276	927	1504	76	1155	1010	1699	1814	1224	0	0	0	3150	937	0
i9	0	0	0	0	0	0	230	89	0	0	767	0	0	0	0	0

Table S5. The set of fitted Weibull shape parameters η_{ij} for the transitions from species i to j.

	i1	**i2**	**i3**	**i12**	**m1**	**i11**	**i4**	**i5**	**i6**	**i8**	**i10**	**i9**	**p1**	**p2**	**p3**	**p4**
i1	0.00	1.64	1.42	1.26	0.95	1.61	1.80	1.96	3.35	0.00	1.64	0.00	0.00	1.07	0.71	0.00
i2	1.73	0.00	1.55	2.02	2.73	0.00	2.20	0.95	0.70	0.00	2.29	0.00	0.00	0.66	0.00	0.00
i3	1.44	1.45	0.00	2.15	1.23	1.30	1.28	2.18	0.00	0.00	2.18	0.00	0.96	0.00	0.00	0.00
i12	1.25	1.91	1.95	0.00	1.42	1.60	1.45	1.43	3.08	2.25	0.92	1.65	0.00	0.00	0.00	3.21
***m*1**	0.89	1.61	1.16	1.31	0.00	1.13	1.27	2.18	0.00	0.00	1.83	0.00	1.89	0.00	0.00	0.00
i11	1.66	0.00	1.75	1.49	1.16	0.00	1.21	1.89	1.17	1.10	0.83	0.00	1.54	0.00	0.00	1.37
***i*4**	2.51	1.98	1.29	1.57	1.93	1.14	0.00	1.57	1.48	1.21	1.43	0.00	0.91	0.00	0.00	3.65
***i*5**	1.49	1.04	1.54	1.18	2.29	1.52	1.14	0.00	0.90	1.27	1.31	0.85	0.00	0.72	0.00	0.00
***i*6**	1.54	1.59	0.00	1.73	0.00	1.92	1.73	0.91	0.00	2.11	2.29	0.00	0.00	0.00	0.00	0.00
***i*8**	0.00	3.49	2.98	2.56	0.00	1.13	1.02	1.53	1.27	0.00	1.38	0.00	1.09	0.00	0.00	0.00
***i*10**	1.00	1.26	2.19	0.94	2.60	0.72	0.81	1.10	1.28	1.00	0.00	0.00	0.00	1.59	0.65	0.00
***i*9**	0.00	0.00	0.00	0.00	0.00	0.00	1.61	1.43	0.00	0.00	2.76	0.00	0.00	0.00	0.00	0.00

When intermediate lifetimes f_{ij} are no longer well-described by simple decaying exponentials ($\eta_{ij} = 1$), the model is no longer Markov, but instead semi-Markov. The steady state solution of a semi-Markov model described by the transition probabilities p_{ij} and Weibull parameters τ_{ij}, η_{ij} can be solved for with a procedure as described by Warr and Collins.[36] A derivation is given here, rewritten for clarity in our notation. Two intermediate properties of interest must be defined: (1), the effective lifetime distributions $q_{ij}(t)$ and (2), the first-passage time distributions $g_{ij}(t)$. They can be related as a set of coupled equations, $q(t)$ and $g(t)$ with subscripts dropped to indicate their use in matrix form, as well as through Laplace transforms, L, as:

$$q_{ij}(t) = p_{ij} f_{ij}(t)$$

$$q^*(s) = L[q(t)] = \int_0^\infty q(t)\exp(-st)dt$$

$$g^*(s) = q^*(s)\left(I - q^*(s)\right)^{-1}\left[I \circ \left(I - q^*(s)\right)^{-1}\right]^{-1}$$

$$G(t) = L^{-1}\left[G^*(s)\right] = L^{-1}\left[\frac{1}{s}g^*(s)\right]$$

The stationary states π_{ij} for a system with absorbing states (the products) can then be simply expressed as:

$$\pi_{ij} = \lim_{t \to \infty} P_{ij}(t) = G_{ij}(\alpha)$$

for a large value of α. Solving for the stationary states requires solving for $G(t)$, which requires an inverse Laplace transform. No single algorithm can reliably solve the inverse Laplace transform $G(t)$ for all possible input functions $G^*(s)$.[37] The function $G(t)$ can be estimated by fitting a solution of the form:

$$G(t_k) \approx \sum_{m=1}^{N_s} w_m \exp\left(-t_k s_m\right) G^*(s_m)$$

over multiple times t_k and N_s possible frequencies, as well as constraints that $G^*(s_m) \geq 0$.[38] Computationally, this can be solved as a RNNLS problem, as described in the computational methods. The steady state solutions computed using this method are shown in Table S6, below.

Table S6. Steady state solutions (i.e., product branching ratios) are shown per starting species for the semi-Markov model, with probabilities represented as percentages.

	p1	**p2**	**p3**	**p4**
i1	64.52	22.77	2.16	10.55
i2	43.26	47.96	1.37	7.41
i3	78.54	14.07	1.19	6.19
i12	61.12	24.11	2.12	12.64
m1	70.12	19.19	1.79	8.90
i11	58.27	20.57	2.04	19.13
i4	61.84	21.25	1.87	15.03
i5	55.73	28.33	2.16	13.78
i6	60.30	21.63	1.98	16.09
i8	61.59	19.69	1.92	16.79
i10	55.85	25.26	2.81	16.08
i9	55.72	28.33	2.16	13.80

Quasi-Atomic Orbital Analysis of SiC_3 Isomers

To elucidate the nature of chemical bonds in SiC_3 isomers in the present work, the quasi-atomic orbital (QUAO) analysis was employed. Briefly, quasi-atomic orbitals can be thought of as distorted atomic minimal basis set orbitals resulting from the bonding formation in a molecule.[23,24,39-42] The QUAO analysis provides quantitative information about the types of bonding interaction, electron populations, bond order (BO), and the kinetic bond order (KBO), which indicates the strength of chemical bonding.[24,33,41] The QUAO pair interactions between two atomic centers of the three isomers are depicted in Fig. S10, while the BOs, KBOs, and electron populations from QUAO analysis are tabulated in Table S7. The QUAO at each atom center is labelled as follows:

- The first letter is the atomic symbol on which the orbital is located.
- If the QUAO participates in bonding, the symbol of a complementary atom is listed as a subscript.
- The Greek letter indicates the bonding types, e.g., sigma and pi orbitals.
- If the QUAO electron populations are close to 2, they are a lone pair (LP).

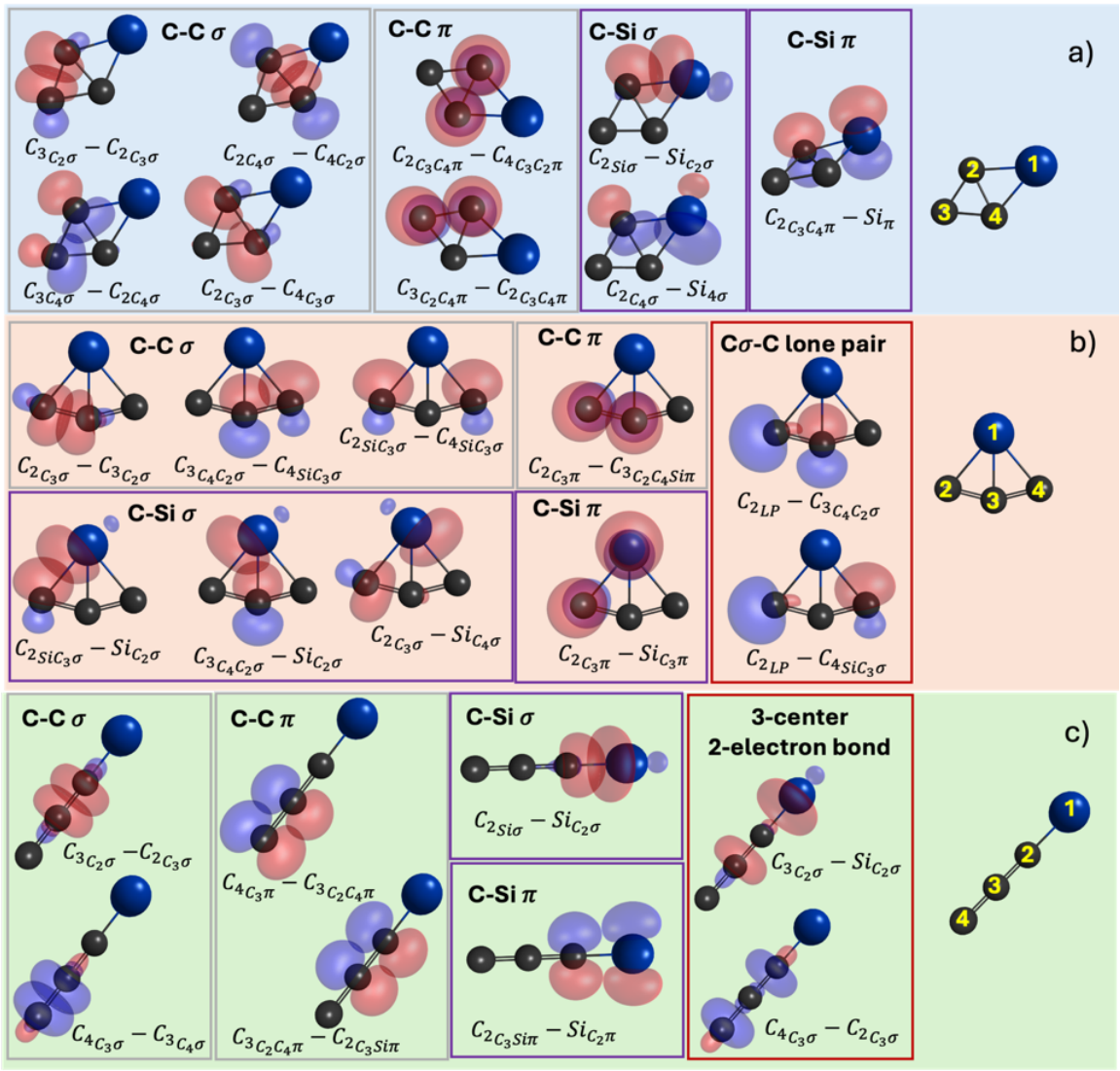

Fig. S10. Quasi-atomic orbitals (QUAOs) of **p1-p3 (a–c)** at the ROHF/cc-pV(T+d)Z//TPSSh/cc-pV(T+d)Z level of theory. The orbital labels are shown below the corresponding bonding interactions, where the atom numbers of each isomer are depicted on the right. Only symmetry-unique QUAOs are demonstrated.

Table S7. Kinetic bond order (KBO), bond order (BO), and occupations (Occ.) of the QUAO pairs of three SiC_3 isomers (compounds **p1-p3**). Only interactions with BO > 0.1 and KBO > −1 kcal/mol.

QUAO pair (I-J)	Occ_I	Occ_J	Interaction type	KBO (kcal/mol)	BO	# symm. eq.[a]	% weighted KBO contribution[b]
Compound **p1**							
$C_{3C_2\sigma} - C_{2C_3\sigma}$	0.87	1.13	C-C σ	-42.62	0.95	2	43%
$C_{2Si\sigma} - Si_{C_2\sigma}$	1.47	0.56	C-Si σ	-22.84	0.85	2	23%
$C_{2C_4\sigma} - C_{4C_2\sigma}$	1.00	1.00	C-C σ	-27.29	-0.89	1	14%
$C_{3C_2C_4\pi} - C_{2C_3C_4\pi}$	0.38	0.72	C-C π	-8.27	0.53	2	8%
$C_{2C_3C_4\pi} - Si_{\pi}$	0.72	0.17	C-Si π	-3.51	0.35	2	4%
$C_{2C_3C_4\pi} - C_{4C_3C_2\pi}$	0.72	0.72	C-C π	-9.47	0.72	1	5%
$C_{3C_4\sigma} - C_{2C_4\sigma}$	0.87	1.00	C-C σ	-2.48	0.25	2	2%
$C_{2C_4\sigma} - Si_{4\sigma}$	1.00	0.56	C-Si σ	-0.91	0.19	2	1%
$C_{2C_3\sigma} - C_{4C_3\sigma}$	1.13	1.13	C-C σ	-1.52	-0.12	1	1%
Compound **p2**							
$C_{2C_3\sigma} - C_{3C_2\sigma}$	0.91	1.09	C-C σ	-52.8	0.98	2	53%
$C_{2SiC_3\sigma} - Si_{C_2\sigma}$	1.09	0.59	C-Si σ	-16.69	0.77	2	17%
$C_{2C_3\pi} - C_{3C_2C_4Si\pi}$	0.33	1.12	C-C π	-12.88	0.61	2	13%
$C_{3C_4C_2\sigma} - C_{4SiC_3\sigma}$	0.91	1.09	C-C σ	-7.93	0.49	2	8%
$C_{2LP} - C_{3C_4C_2\sigma}$	1.91	0.91	Cσ -C LP	-2.3	0.3	2	2%
$C_{2C_3\pi} - Si_{C_3\pi}$	0.33	0.22	C-Si π	-2.04	0.27	2	2%
$C_{3C_4C_2\sigma} - Si_{C_2\sigma}$	0.91	0.59	C-Si σ	-1.88	0.36	2	2%
$C_{2C_3\sigma} - Si_{C_4\sigma}$	0.91	0.59	C-Si σ	-1.51	-0.15	2	2%
$C_{2SiC_3\sigma} - C_{4SiC_3\sigma}$	1.09	1.09	C-C σ	-1.38	-0.22	1	1%
$C_{2LP} - C_{4SiC_3\sigma}$	1.91	1.09	Cσ -C LP	-1.18	-0.2	2	1%

[a] Symmetry equivalent

[b] The percent weighted KBO contribution was determined as a ratio of $(KBO_i \times \#\ symm\ equivalent)$ and $\sum_i (KBO_i \times \#\ symm\ equivalent)$

Table S7. Continued.

QUAO pair (I-J)	Occ_I	Occ_J	Interaction type	KBO (kcal/mol)	BO	# symm. eq.[a]	% weighted KBO contribution[b]
Compound **p3**							
$C_{3C_2\sigma} - C_{2C_3\sigma}$	1.02	1.00	C-C σ	-66.24	0.98	1	28%
$C_{4C_3\sigma} - C_{3C_4\sigma}$	0.94	1.06	C-C σ	-59.11	0.99	1	25%
$C_{2Si\sigma} - Si_{C_2\sigma}$	1.37	0.63	C-Si σ	-24.98	0.92	1	11%
$C_{4C_3\pi} - C_{3C_2C_4\pi}$	0.57	0.99	C-C π	-16.13	0.65	2	14%
$C_{2C_3Si\pi} - Si_{C_2\pi}$	1.02	0.41	C-Si π	-9.47	0.57	2	8%
$C_{3C_2C_4\pi} - C_{2C_3Si\pi}$	0.99	1.02	C-C π	-14.5	0.66	2	12%
$C_{3C_2\sigma} - Si_{C_2\sigma}$	0.94	1.00	3-c-2e	-3.45	-0.12	1	1%
$C_{4C_3\sigma} - C_{2C_3\sigma}$	1.02	0.63	3-c-2e	-2.09	0.1	1	1%

[a] Symmetry equivalent

[b] The percent weighted KBO contribution was determined as a ratio of $(KBO_i \times \#\ symm\ equivalent)$ and $\sum_i (KBO_i \times \#\ symm\ equivalent)$

Data S1. Properties of all species. Optimized Cartesian coordinates (Å) and vibrational frequencies (cm^{-1}) of reactants, products, intermediates, and transition states involved in the Tricarbon (C_3) plus silylidyne (SiH) reaction.

-- REACTANTS --

C3

C	-7.9865254668	1.1814275949	0.0000000000
C	-6.7843420529	1.6566215469	0.0000000000
C	-5.5820224803	2.1314708582	0.0000000000

Wavenumber
[1/cm]
57.87
1221.02
2119.62

SiH

Si	-7.6498736128	2.1391367463	0.0000000000
H	-6.2527163872	2.7546932537	0.0000000000

Wavenumber
[1/cm]
2031.11

-- PRODUCTS --

p1

Si	0.8164860655	1.1398022796	0.0000000000
C	-1.0231427326	1.1913157714	0.0000000000
C	-1.8861466287	0.0430854531	0.0000000000
C	-0.4669767042	-0.1791735041	0.0000000000

Wavenumber
[1/cm]
209.69
413.72
679.43
1007.86
1056.17
1393.16

p2

Si	-5.1772103509	3.7540258069	0.0000000000
C	-6.4825908081	2.1897013309	0.0000000000
C	-5.1799505350	1.8598596469	0.0000000000
C	-3.8763483060	2.1859032153	0.0000000000

Wavenumber
[1/cm]
124.36
411.47
506.75
797.49
1134.56
1567.34

p3

Si	1.0712387723	0.9955755089	0.0000000000
C	1.0567906544	-0.7433202879	0.0000000000
C	1.0458962832	-2.0331201678	0.0000000000
C	1.0344242900	-3.3400050531	0.0000000000

Wavenumber
[1/cm]
118.06
283.44
456.93
612.09
1318.81
1986.73

p4

H	0.9215703138	-1.5203308186	0.0362965118
C	0.4555296953	-0.6506870748	0.4781191896
C	-0.3487110480	-0.0902527314	1.4381590080
C	0.2401054563	0.7047207529	0.4905009945

Wavenumber
[1/cm]
523.23
878.83
913.60
1229.65
1596.70
3216.63

p5

Si	0.1948666145	-0.0221863540	-0.0345382783
C	1.8343224758	-0.8160771492	-0.1423530639
C	1.9094685103	0.4403556366	-0.4520629496
C	-1.5977456005	0.1531018666	0.2585052919

Wavenumber
[1/cm]
103.49
139.07
444.53
638.38
918.50
1626.40

-- INTERMEDIATES --

i1

Si	1.5066421261	1.1239293774	0.6272363910
C	1.1508729089	-0.5386371836	0.1339523687
C	1.0314227555	-1.8040559818	-0.0234246075
C	0.8699644134	-3.0801820437	-0.2413589670
H	0.7207747961	1.7202198318	-0.5152421852

Wavenumber
[1/cm]

139.70
151.84
328.11
389.42
569.44
703.94
1318.62
1967.37
2089.28

iS2			
Si	0.0179052241	0.7933027795	0.7143231245
C	-1.0780697910	-0.7350810398	0.1587489923
C	-0.0160069541	-1.1195734104	-0.5835987920
C	1.0794341813	-0.7417556557	0.1122274407
H	-0.0032626603	1.8031073264	-0.4017007655

Wavenumber
[1/cm]
312.22
373.60
467.48
499.25
605.18
718.64
1239.25
1314.14
2103.59

i3			
Si	0.9024468374	1.1938776018	0.7977470932
C	-0.9080036613	1.2647752327	0.0370737375
C	-1.5686304908	0.1647520225	-0.3783180851
C	-0.3272128986	-0.1432769686	0.0495510695
H	1.5449402133	1.4466341116	-0.5482318152

Wavenumber
[1/cm]
318.71
331.83
496.79
628.69
700.82
868.35
1191.94
1586.82
2071.92

i4			
Si	-0.4523084176	0.4396598719	-1.0495637040
H	1.0048895546	-1.5498645154	0.2163850276
C	0.2515003893	-0.7677208189	0.1951824650
C	-0.2152945972	-0.1148159882	1.4144110065
C	0.2273990708	0.8758514506	0.6170972048

Wavenumber
[1/cm]
153.14

445.28
573.95
760.24
802.09
901.83
1063.28
1408.94
3129.28

i5			
Si	0.0063428176	-0.9017098576	0.2068944827
H	-1.8601692992	1.2700009658	0.0420651979
C	0.3558577294	0.9307646758	-0.2838948403
C	-0.9594385669	0.6797528351	0.0148524499
C	1.5283764190	0.3366176809	-0.3594966903

Wavenumber
[1/cm]
336.39
384.15
426.73
610.95
737.90
939.48
1153.60
1559.13
3255.12

i6			
Si	-0.2603023763	-0.7239408758	0.5905165567
H	0.3471229455	1.5939650255	-1.0144285856
C	-1.1092505314	0.2344815636	-0.7379361902
C	0.3340568825	0.7536877933	-0.3077129707
C	1.3317739798	0.4265373934	0.5733910898

Wavenumber
[1/cm]
284.56
288.71
434.58
588.64
611.94
772.78
797.95
1208.59
3053.57

i7			
Si	0.2941659514	1.1531195396	-0.3978510851
H	-0.5382194840	-2.1879647395	-0.2346160109
C	0.8200319609	-0.4426013102	0.4134003087
C	-0.9898015478	0.0037695487	0.3174669509
C	-0.3047050805	-1.1747837386	0.0682840364

Wavenumber
[1/cm]
319.75
498.54

541.96
803.16
881.95
936.56
1137.03
1431.80
3184.28

i8			
Si	1.1133511469	0.6111945578	-0.2579024307
H	-2.2739849196	-1.2546235380	0.5280402373
C	-1.3515025788	-0.7465911531	0.3142644800
C	-0.7502410529	0.3942579328	-0.1629726391
C	0.0224335044	-0.7992623995	0.3335442525

Wavenumber
[1/cm]
362.96
369.81
542.85
622.50
910.07
969.92
1028.46
1486.00
3284.65

i10			
Si	1.7973052824	-0.0000008755	-0.0000013916
H	-3.5236755081	-0.0000029384	-0.0000031514
C	-2.4604634539	0.0000034597	0.0000039187
C	-1.2269436194	0.0000003533	-0.0000007104
C	0.1005836990	0.0000001009	0.0000014347

Wavenumber
[1/cm]
153.56
174.48
381.74
445.93
517.50
630.13
636.17
1446.68
1966.45
3449.80

i11			
Si	0.8492944715	-1.2374288444	-0.7975983924
H	-2.0298599248	0.7554426330	0.5047151174
C	0.2143024518	1.4099200157	0.8783905399
C	0.1792448619	0.1506727373	0.0867150402
C	-0.9538969604	0.8176883583	0.5255776949

Wavenumber
[1/cm]
139.82
319.23

562.14
820.23
880.94
961.04
1131.86
1566.57
3247.13

i9			
Si	-0.1333184476	-0.4225593319	-0.0115153498
H	1.9902784287	-1.9881822359	-0.1633026006
C	-1.8292824592	0.2095910975	0.2029844184
C	1.4048942406	-1.0828089803	-0.1935238835
C	-1.0133547626	1.1593294507	-0.0932875845

Wavenumber
[1/cm]
128.94
177.34
368.34
384.38
489.72
707.64
1101.13
1686.65
3271.03

i12			
Si	1.8757474196	0.4119971818	0.5067669689
H	0.9162213420	-0.6048775911	-0.7403524923
C	-2.3354538732	-0.2095198917	-0.2577557126
C	-1.0602556172	-0.1137585364	-0.1392780852
C	0.2608567288	0.0146478374	0.0188253212

Wavenumber
[1/cm]
146.31
147.36
337.70
368.05
601.04
1050.80
1293.18
1968.91
2329.99

-- TRANSITION STATES --

i4-i5			
Si	-0.3464411751	0.4421440165	-1.1865399025
H	0.9136761417	-1.5469302127	0.2197240202
C	0.2654017610	-0.6919618116	0.0889966395
C	-0.0571180152	-0.0758117603	1.6402832054
C	0.0406662876	0.7556697681	0.6310480373

Wavenumber
[1/cm]
304.43
470.63
640.93
736.48
862.31
962.89
1586.54
3201.22

Imaginary frequency
509.05

i4-i7			
Si	0.6387302167	1.3594221071	-0.8185207696
H	-0.3287404883	-1.5034823622	-0.5120624270
C	-0.8634252730	0.3294458628	0.7815397097
C	-0.2496782826	-0.5314015150	-0.0469254290
C	0.8031138272	0.3460169073	0.5959679159

Wavenumber
[1/cm]
318.39
483.86
787.82
866.33
919.12
1022.74
1486.01
3207.62

Imaginary frequency
502.42

i4-i11			
Si	-0.5259222964	0.7853156248	-1.4823847635
H	0.7948867398	-1.3289934868	-0.1214672074
C	0.0912709736	-0.5321938550	0.0871172150
C	-0.2388757395	0.0860149806	1.3038672604
C	-0.1213596776	0.9898567364	0.2128674955

Wavenumber
[1/cm]
300.68
436.31
734.75
814.42
868.41
988.79
1357.95
3163.64

Imaginary frequency
782.09

i5-i6			
Si	0.3375854600	-1.3960471037	0.2612808080

C	1.4491665529	0.1915072562	-0.3075883217
C	0.1386817960	0.3811466736	-0.1133046862
C	-1.2063887385	-0.3159970490	0.2926571113
H	-0.7190450704	1.1393902228	-0.1330449114

Wavenumber
[1/cm]
329.37
359.71
510.05
573.90
712.57
832.62
1318.94
2645.11

Imaginary frequency
685.03

i5-i10

Si	0.9296738387	-1.7926180984	0.1924733810
H	-1.7894792096	1.1529780722	-0.0837088367
C	-0.9379605071	0.5656755000	0.1944095529
C	0.2772240138	0.2813028093	-0.0535304783
C	1.5205418642	-0.2073382830	-0.2496436189

Wavenumber
[1/cm]
191.59
407.75
433.77
495.66
854.81
1129.45
1724.23
3343.12

Imaginary frequency
454.71

i5-i9

Si	0.1627348670	-0.9477177285	0.1903817611
C	1.8480129069	-0.5008931057	-0.2196698269
C	1.2815862994	0.6605678516	-0.3887833320
C	-1.1314755297	0.2304557199	0.1521789275
H	-2.1608585436	0.5575872627	0.2658924703

Wavenumber
[1/cm]
231.20
349.49
426.17
707.48
770.72
877.84
1590.87
3192.32

Imaginary frequency

282.29

i6-i7

Si	0.3372754681	-1.3850231883	0.4165762818
C	1.3257146330	0.1347531207	-0.4075281063
C	0.0280511668	0.3929500632	-0.0999997782
C	-1.2586429165	-0.5284013911	0.2130194102
H	-0.4323983513	1.3857213954	-0.1220678075

Wavenumber
[1/cm]
365.51
442.79
578.83
659.95
749.22
831.65
1274.26
3075.59

Imaginary frequency
489.18

i7-i8

Si	0.4174536285	1.8005066100	-0.3424861256
H	-0.4218282803	-1.7169202021	-0.1839135647
C	-0.7917414343	0.5575970170	0.1891343637
C	-0.1452187162	-0.6931397527	0.0260060904
C	0.9413348023	0.0519553277	0.3112592362

Wavenumber
[1/cm]
442.97
546.08
779.52
830.94
963.17
1110.06
1484.90
3208.19

Imaginary frequency
528.42

i8-i10

Si	1.9996787846	0.0339414840	-0.5038320773
H	-2.1086678624	-0.0055133388	0.0124811166
C	-1.0588993217	0.0085517194	-0.1789864154
C	0.1741770395	0.0229209275	-0.3728107274
C	0.9937113600	-0.0599017922	1.0431481034

Wavenumber
[1/cm]
242.95
456.39
520.43
548.73
717.75

790.81
1743.94
3414.10

Imaginary frequency
362.23

i8-i11

Si	1.4819516801	-1.4761650772	-0.9537071818
H	-1.7132915900	0.5858428036	0.3973534691
C	0.6224733743	0.8643904288	0.5334033986
C	-0.6508521662	0.4365290898	0.2856164158
C	0.2597177018	-0.4105972450	-0.2626661018

Wavenumber
[1/cm]
305.88
617.77
716.69
776.75
989.43
1237.29
1584.07
3234.71

Imaginary frequency
154.24

i12-i5

Si	1.8018960235	0.4635538808	0.5702703786
H	0.8145691934	-0.8087268669	-0.9896313575
C	-2.2865386188	-0.0927726625	-0.1137285706
C	-1.0078821831	-0.1424819102	-0.1757905850
C	0.3465645849	-0.1648854412	-0.2014968654

Wavenumber
[1/cm]
100.84
289.66
451.69
595.00
1044.12
1226.96
1953.63
2794.64

Imaginary frequency
160.14

i1-i5

Si	0.1091039930	0.8032240218	0.9210391910
C	-1.0636168028	-0.1749287591	-0.1307804503
C	0.0800692735	-0.9010179760	-0.3527548365
C	1.2981030393	-1.1022569049	0.0212572445
H	-0.4236595029	1.3749796182	-0.4587611487

Wavenumber

[1/cm]
72.93
285.96
495.51
644.47
900.65
1138.54
1711.20
1754.18

Imaginary frequency
804.12

i1-i12			
Si	-1.1477077687	1.4018933671	0.8810029864
C	-0.2551921999	0.0180158800	0.2933595462
C	0.4395750515	-0.9661490259	-0.1949648731
C	1.1053545747	-1.9815745537	-0.6389036581
H	-0.1420296576	1.5278143326	-0.3404940014

Wavenumber
[1/cm]
149.07
160.03
366.31
490.45
612.60
1330.82
1866.67
1987.51

Imaginary frequency
719.90

i1-i2			
Si	0.7853581101	0.8498865649	-0.0830512440
C	-0.3513451593	-0.0380481038	1.1797391372
C	-0.4167737242	-1.0028553208	0.2628576943
C	0.3768187023	-1.4151523488	-0.6953748141
H	-0.3940579289	1.6061692084	-0.6641707734

Wavenumber
[1/cm]
220.68
391.17
549.56
593.62
707.90
1260.02
1596.35
2042.55

Imaginary frequency
187.19

i1-i3			
Si	0.7042494401	1.3873505919	0.4554086525
C	-0.1757223358	-0.1551847315	0.2234950936

C	-0.6849566217	-1.3761869958	0.1892895785
C	0.3819189069	-1.9230764336	-0.3426717221
H	-0.2254893895	2.0670975690	-0.5255216026

Wavenumber
[1/cm]
145.41
266.91
288.08
606.53
704.31
1549.67
1626.02
2074.79

Imaginary frequency
449.30

i2-i5

Si	0.1097364117	0.7981120218	0.9216018652
H	-0.4272091533	1.3754086676	-0.4539128671
C	-1.0646579902	-0.1791677544	-0.1311013922
C	0.0815530798	-0.9009022145	-0.3561822240
C	1.3005776520	-1.0934507206	0.0195946180

Wavenumber
[1/cm]
81.35
286.38
496.40
642.10
900.54
1138.77
1708.87
1755.12

Imaginary frequency
802.67

i2-i3

Si	-0.0412522002	0.8691917641	0.7578718982
C	-0.9726830983	-0.8280483029	0.1871055702
C	-0.0425314686	-1.3035524438	-0.6351080463
C	0.9128688215	-0.5768332113	0.0675448529
H	0.1435979457	1.8392421940	-0.3774142750

Wavenumber
[1/cm]
346.46
411.22
534.66
592.80
664.22
1107.31
1422.74
2099.75

Imaginary frequency
1041.30

i3-i4

Si	0.0169776837	0.0488340451	-1.1865683088
H	0.9784050664	-1.0559255068	-0.3275809115
C	-0.1620357540	-0.7508186153	0.4067974417
C	0.0646778549	-0.1070761391	1.6619575091
C	-0.0150523916	0.8188892421	0.7336694134

Wavenumber
[1/cm]
303.09
364.08
484.14
773.25
998.32
1156.64
1530.61
1648.47

Imaginary frequency
994.25

Supplementary References

1 X. Gu, Y. Guo and R. I. Kaiser, *Int. J. Mass Spectrom.*, 2005, **246**, 29-34.

2 T. Yang, B. B. Dangi, P. Maksyutenko, R. I. Kaiser, L. W. Bertels and M. Head-Gordon, *J. Phys. Chem. A*, 2015, **119**, 12562-12578.

3 N. Tada, K. Tonokura, K. Matsumoto, M. Koshi, A. Miyoshi and H. Matsui, *J. Phys. Chem. A*, 1999, **103**, 322-329.

4 Y. Muranaka, T. Motooka, D. Lubben and J. E. Greene, *J. Appl. Phys.*, 1989, **66**, 910-914.

5 M. F. Vernon, Ph.D. Dissertation, University of California at Berkeley, 1983.

6 P. S. Weiss, Ph.D. Dissertation, University of California at Berkeley, 1985.

7 R. I. Kaiser, *Chem. Rev.*, 2002, **102**, 1309-1358.

8 H. J. Werner, P. J. Knowles, G. Knizia, F. R. Manby, M. Schütz, P. Celani, W. Györffy, D. Kats, T. Korona, R. Lindh, A. Mitrushenkov, G. Rauhut, K. R. Shamasundar, T. B. Adler, R. D. Amos, A. Bernhardsson, A. Berning, D. L. Cooper, J. O. Deegan, A. J. Dobbyn, F. Eckert, E. Goll, C. Hampel, A. Hesselmann, G. Hetzer, T. Hrenar, G. Jansen, C. Köppl, Y. Liu, A. W. Lloyd, R. A. Mata, A. J. May, S. J. McNicholas, W. Meyer, M. E. Mura, A. Nicklass, D. P. O'Neill, P. Palmieri, D. Peng, K. Pflüger, R. Pitzer, M. Reiher, T. Shiozaki, H. Stoll, A. J. Stone, R. Tarroni, T. Thorsteinsson and M. Wang, *MOLPRO, a package of ab initio programs*, *Version 2015.1*, University of Cardiff, Cardiff, UK, 2015.

9 L. Zhao, T. Yang, R. I. Kaiser, T. P. Troy, B. Xu, M. Ahmed, J. Alarcon, D. Belisario-Lara, A. M. Mebel, Y. Zhang, C. Cao and J. Zou, *Phys. Chem. Chem. Phys.*, 2017, **19**, 15780-15807.

10 T. H. Dunning Jr., K. A. Peterson and A. K. Wilson, *J. Chem. Phys.*, 2001, **114**, 9244-9253.

11 T. B. Adler, G. Knizia and H.-J. Werner, *J. Chem. Phys.*, 2007, **127**, 221106.

12 G. Knizia, T. B. Adler and H.-J. Werner, *J. Chem. Phys.*, 2009, **130**, 054104.

13 K. Fujioka, J. Waldrop, R. Richard, Y. Luo, T. Windus and R. Sun, *ChemRxiv*, 2025, DOI: 10.26434/chemrxiv-2025-ch56h.

14 R. M. Parrish, L. A. Burns, D. G. A. Smith, A. C. Simmonett, A. E. DePrince, III, E. G. Hohenstein, U. Bozkaya, A. Y. Sokolov, R. Di Remigio, R. M. Richard, J. F. Gonthier, A. M. James, H. R. McAlexander, A. Kumar, M. Saitow, X. Wang, B. P. Pritchard, P. Verma, H. F. Schaefer, III, K. Patkowski, R. A. King, E. F. Valeev, F. A. Evangelista, J. M. Turney, T. D. Crawford and C. D. Sherrill, *J. Chem. Theory Comput.*, 2017, **13**, 3185-3197.

15 R. Peverati and D. G. Truhlar, *J. Phys. Chem. Lett.*, 2011, **2**, 2810-2817.

16 T. H. Dunning Jr., *J. Chem. Phys.*, 1989, **90**, 1007-1023.

17 D. E. Woon and T. H. Dunning, Jr., *J. Chem. Phys.*, 1993, **98**, 1358-1371.

18 K. Fujioka, E. Lam, B. Loi and R. Sun, *Carbon Trends*, 2023, **11**, 100257.

19 S. Chmiela, H. E. Sauceda, I. Poltavsky, K.-R. Müller and A. Tkatchenko, *Comput. Phys. Commun.*, 2019, **240**, 38-45.

20 S. R. Heller, A. McNaught, I. Pletnev, S. Stein and D. Tchekhovskoi, *J. Cheminf.*, 2015, **7**, 23.

21 N. M. O'Boyle, M. Banck, C. A. James, C. Morley, T. Vandermeersch and G. R. Hutchison, *J. Cheminf.*, 2011, **3**, 33.

22 S. W. Provencher, *Comput. Phys. Commun.*, 1982, **27**, 213-227.

23 A. C. West, M. W. Schmidt, M. S. Gordon and K. Ruedenberg, *J. Chem. Phys.*, 2013, **139**.

24 A. C. West, M. W. Schmidt, M. S. Gordon and K. Ruedenberg, *J. Phys. Chem. A*, 2015, **119**, 10360-10367.

25 A. C. West, M. W. Schmidt, M. S. Gordon and K. Ruedenberg, *J. Phys. Chem. A*, 2017, **121**, 1086-1105.

26 K. Ruedenberg, *J. Chem. Phys.*, 2022, **157**.

27 M. W. Schmidt, K. K. Baldridge, J. A. Boatz, S. T. Elbert, M. S. Gordon, J. H. Jensen, S. Koseki, N. Matsunaga, K. A. Nguyen and S. Su, *J. Comput. Chem.*, 1993, **14**, 1347-1363.

28 M. S. Gordon and M. W. Schmidt, in *Theory and Applications of Computational Chemistry*, eds. C. E. Dykstra, G. Frenking, K. S. Kim and G. E. Scuseria, Elsevier, Amsterdam, 2005, DOI: https://doi.org/10.1016/B978-044451719-7/50084-6, pp. 1167-1189.

29 G. M. J. Barca, C. Bertoni, L. Carrington, D. Datta, N. De Silva, J. E. Deustua, D. G. Fedorov, J. R. Gour, A. O. Gunina, E. Guidez, T. Harville, S. Irle, J. Ivanic, K. Kowalski, S. S. Leang, H. Li, W. Li, J. J. Lutz, I. Magoulas, J. Mato, V. Mironov, H. Nakata, B. Q. Pham, P. Piecuch, D. Poole, S. R. Pruitt, A. P. Rendell, L. B. Roskop, K. Ruedenberg, T. Sattasathuchana, M. W. Schmidt, J. Shen, L. Slipchenko, M. Sosonkina, V. Sundriyal, A. Tiwari, J. L. Galvez Vallejo, B. Westheimer, M. Włoch, P. Xu, F. Zahariev and M. S. Gordon, *J. Chem. Phys.*, 2020, **152**.

30 F. Zahariev, P. Xu, B. M. Westheimer, S. Webb, J. Galvez Vallejo, A. Tiwari, V. Sundriyal, M. Sosonkina, J. Shen, G. Schoendorff, M. Schlinsog, T. Sattasathuchana, K. Ruedenberg, L. B. Roskop, A. P. Rendell, D. Poole, P. Piecuch, B. Q. Pham, V. Mironov, J. Mato, S. Leonard, S. S. Leang, J. Ivanic, J. Hayes, T. Harville, K. Gururangan, E. Guidez, I. S. Gerasimov, C. Friedl, K. N. Ferreras, G. Elliott, D. Datta, D. D. A. Cruz, L. Carrington, C. Bertoni, G. M. J. Barca, M. Alkan and M. S. Gordon, *J. Chem. Theory Comput.*, 2023, **19**, 7031-7055.

31 W. C. Lu, C. Z. Wang, M. W. Schmidt, L. Bytautas, K. M. Ho and K. Ruedenberg, *J. Chem. Phys.*, 2004, **120**, 2629-2637.
32 G. B. Bacskay, S. Nordholm and K. Ruedenberg, *J. Phys. Chem. A*, 2018, **122**, 7880-7893.
33 D. Del Angel Cruz, K. N. Ferreras, T. Harville, G. Schoendorff and M. S. Gordon, *Phys. Chem. Chem. Phys.*, 2024, **26**, 21395-21406.
34 C. He, Z. Yang, S. Doddipatla, A. M. Thomas, R. I. Kaiser, G. R. Galimova, A. M. Mebel, K. Fujioka and R. Sun, *Phys. Chem. Chem. Phys.*, 2022, **24**, 26499-26510.
35 Z. Yang, K. Fujioka, G. R. Galimova, I. A. Medvedkov, S. J. Goettl, R. Sun, A. M. Mebel and R. I. Kaiser, *ACS Cent. Sci.*, 2025, **11**, 322-330.
36 R. L. Warr and D. H. Collins, *Int. J. Simul. Process Model.*, 2015, **10**, 89-99.
37 K. L. Kuhlman, *Numer. Algorithms*, 2013, **63**, 339-355.
38 Z. Cai, *Inverse Laplace transform of real-valued relaxation data by a regularized non-negative least squares method*, Github, 2014.
39 A. C. West, M. W. Schmidt, M. S. Gordon and K. Ruedenberg, *J. Phys. Chem. A*, 2015, **119**, 10368-10375.
40 A. C. West, M. W. Schmidt, M. S. Gordon and K. Ruedenberg, *J. Phys. Chem. A*, 2015, **119**, 10376-10389.
41 A. C. West, J. J. Duchimaza-Heredia, M. S. Gordon and K. Ruedenberg, *J. Phys. Chem. A*, 2017, **121**, 8884-8898.
42 E. B. Guidez, M. S. Gordon and K. Ruedenberg, *J. Am. Chem. Soc.*, 2020, **142**, 13729-13742.